Role of Annealing in Improving Shape Memory Effect of As-Cast Fe-Mn-Si-Cr-Ni Shape Memory Alloys

HUABEI PENG, LIQIU YONG, SHANLING WANG, and YUHUA WEN

The impact of annealing temperature and annealing time on the shape memory effect of an as-cast Fe-18.54Mn-5.70Si-8.91Cr-4.45Ni alloy was investigated by optical metallography, XRD, SEM, TEM, and bending techniques. The recovery strain of the as-cast alloy was only 5.6 pct because a high density of stacking faults was not obtained. The shape memory effect of the as-cast alloy was improved by annealing for 30 minutes at 573 K, 873 K, or 1073 K (300 °C, 600 °C, or 800 °C) as well as at 873 K (600 °C) for 5, 30, or 720 minutes, whereas it deteriorated after annealing at 1373 K (1100 °C) for 30 or 750 minutes. The maximum improvement of the shape memory effect was achieved after annealing at 873 K (600 °C) for 30 minutes because dislocations, derived from low-angle grain boundaries, decomposed into stacking faults. It was concluded that the variation of the shape memory effect with different annealing processes is associated with the evolution of dislocations derived from low-angle grain boundaries for cast Fe-Mn-Si-based shape memory alloys.

I. INTRODUCTION

FE-MN-SI-BASED shape memory alloys (SMAs) are considered for engineering applications because of their good workability, machinability, weldability, damping capacity, and their low cost. Sato et al. first reported that monocrystalline Fe-30Mn-1Si SMA showed an excellent shape memory effect (SME), i.e., an ~ 9 pct recovery strain.[1] However, solution-treated polycrystalline Fe-Mn-Si-based SMAs only achieved a recovery strain of 2 to 3 pct,[2,3] which does not meet the requirements of engineering applications. Many attempts have been made to improve the recovery strain of Fe-Mn-Si-based SMAs, i.e., by tuning the alloy composition,[2,4,5] training,[6,7] thermomechanical treatments,[8–11] ausforming,[12–15] adding interstitial atoms,[16–19] precipitating particles,[20–23] melt spinning,[24] casting,[25–27] and utilizing the $\delta \rightarrow \gamma$ phase transformation.[28] To date, the most successful case is that Wen et al. obtained the bending recovery strain of 8.4 pct and tensile recovery strain of 7.6 pct in an annealed cast polycrystalline Fe-20.2Mn-5.6Si-8.9Cr-5.0Ni alloy.[27] Casting is a cost-efficient manufacturing technique, and it is especially suitable to fabricate components with complex shapes. Thus, cast Fe-Mn-Si-based SMAs are the most favorable for large-scale production.

Although cast Fe-Mn-Si-based SMAs hold great promise for engineering applications, this approach is not attracting worldwide attention from researchers. There are only a small number of post-studies on cast Fe-Mn-Si-based SMAs. For example, Peng et al. investigated the effect of Mn contents on the solidification mode of cast Fe-Mn-Si-based SMAs, and subsequently established a set of Cr_{eq} and Ni_{eq} equations to predict their solidification modes.[29,30] In addition, Wang et al. reported that grain refinement by adding titanium deteriorates the shape memory effect of cast Fe-Mn-Si-based SMAs.[31] Furthermore, Peng et al. demonstrated that coarsening austenitic grains is a key criterion for achieving large recovery strains in cast polycrystalline Fe-Mn-Si-based SMAs.[32] It should be noted that an annealing treatment is a simple way to tailor properties of castings. Wen et al. reported that the evolution of lathy δ-ferrite with an annealing treatment influenced the shape memory effect of a cast Fe-18Mn-5.5-Si-9.5Cr-4Ni SMA.[33] However, the existence of δ-ferrite obscures the effect of annealing treatment on other microstructures in cast Fe-Mn-Si-based SMAs. Therefore, we selected an Fe-18.54Mn-5.70Si-8.91Cr-4.45Ni SMA, which is nearly free of δ-ferrite, to clarify the correlation between annealing treatments and the shape memory effect.

HUABEI PENG, LIQIU YONG, and YUHUA WEN are with the School of Manufacturing Science and Engineering, Sichuan University, Chengdu 610065, P.R. China. Contact e-mail: wenyh@scu.edu.cn SHANLING WANG is with the Analytical and Testing Center, Sichuan University, Chengdu 610065, P.R. China. Contact e-mail: wangshanling@scu.edu.cn
Manuscript submitted November 2, 2018.
Article published online April 22, 2019.

II. EXPERIMENTAL

Ingots with dimensions of 20 mm × 130 mm × 150 mm of an Fe-18.54Mn-5.70Si-8.91Cr-4.45Ni alloy were prepared by melting high purity iron, manganese, silicon, chromium, and nickel in an induction furnace in an argon atmosphere. As-cast specimens were cut directly from the ingots by wire electrical discharge machining. Then, the as-cast specimens were annealed at different temperatures for different times.

The shape memory effect was determined by a conventional bending technique, as described in our previous paper.[34] Specimens with a thickness of 1.5 mm were deformed at M_s + 10 K. To satisfy the deformation temperature requirement, the phase transformation temperatures were determined by resistivity–temperature curves. Table I gives the phase transformation temperatures of as-cast specimens before and after annealing at different temperatures for different times. For metallographic observation, specimens were first mechanically ground, electropolished in an electrolyte consisting of 10 pct perchloric acid and 90 pct ethanol and etched by a tint etchant of 1.2 pct potassium metabisulfite and 0.5 pct ammonium bifluoride in distilled water. In the color optical micrographs, γ-austenite is brown and ε-martensite is white except for thin plates that appear as dark lines. In addition, microstructures were also observed by scanning electron microscopy (SEM) on an S-4800 instrument equipped with energy-dispersive spectrometry (EDS) as well as transmission electron microscopy (TEM) on a Tecnai G2 F20 instrument. TEM specimens were ground mechanically into thin foils of approximately 80 μm, punched into circles with a diameter of 3 mm, and then electropolished using a twin jet polisher in a solution of sulfuric acid and methanol (1:4) until a hole appeared in the center. Specimens were also characterized by electronic backscatter diffraction (EBSD) in a JEOL 6500 F scanning electron microscope. The EBSD scan step was 5 or 10 μm. The tolerance for the twin misorientation was set at 5 deg. The misorientation of low-angle grain boundaries was less than 15 deg, and the misorientation of high-angle grain boundaries was larger than 15 deg. Phases of γ-austenite and ε-martensite were determined

using a Philips X'Pert Pro MPD X-ray diffraction (XRD) apparatus with a Cu target. The XRD scan rate was 6 deg/min. The stacking fault probability is directly proportional to the density of stacking faults. Thus, two austenitic diffraction peaks, i.e., $(111)_\gamma$ and $(200)_\gamma$, were scanned at 0.6 deg/min and used to calculate the stacking fault probability by the X-ray peak shift method described in Reference 35. Specimens for XRD were ground mechanically and then electropolished by a solution of perchloric acid and ethyl alcohol (1:9).

Generally, the volume fraction of ε-martensite can be calculated using XRD results. However, the intensity of diffraction peaks is influenced by the grain size of the material. In other words, the diffraction pattern may be irregular if the grain size is large enough. Therefore, the volume fraction of ε-martensite cannot be determined by XRD due to the coarse grains of cast alloys. In this case, we used a manual point counting method to measure the volume fraction of ε-martensite.[32] First, Analysis Five software (Olympus, Japan) was used to form a montage of optical micrographs to create high-resolution large-area images. Next, an array of one thousand points was formed by a grid that consisted of equally spaced points formed by the intersection of fine lines. This grid was then superimposed upon the high-resolution large-area images. The volume fraction of ε-martensite equaled the number of points falling on the ε-martensite divided by the total number of points in the array.

III. RESULTS

A. Effect of Annealing Parameters on Microstructures

Figure 1 shows color optical micrographs of as-cast specimens before and after annealing at different temperatures for 30 minutes. The obvious microstructure differences were not observed for the cast specimens annealed from 573 K to 1373 K (300 °C to 1100 °C) for 30 minutes. However, austenitic grains formed regular polygons after annealing at 1373 K (1100 °C) for 750 minutes.

Table I. Phase Transformation Temperatures of As-Cast Specimens Before and After Annealing at Different Temperatures for Different Times

Heat Treatment	Phase Transformation Temperature (K)		
	M_s	A_s	A_f
As-Cast	263	355	405
Annealing at 573 K (300 °C) for 30 min	278	348	398
Annealing at 873 K (600 °C) for 5 min	283	363	414
Annealing at 873 K (600 °C) for 30 min	284	361	406
Annealing At 873 K (600 °C) For 720 min	289	360	403
Annealing at 1073 K (800 °C) for 30 min	276	372	425
Annealing at 1373 K (1100 °C) for 30 min	282	373	429
Annealing at 1373 K (1100 °C) for 750 min	280	375	413

M_s the starting temperature of martensitic transformation, A_s the starting temperature of reverse martensitic transformation, A_f the finishing temperature of reverse martensitic transformation.
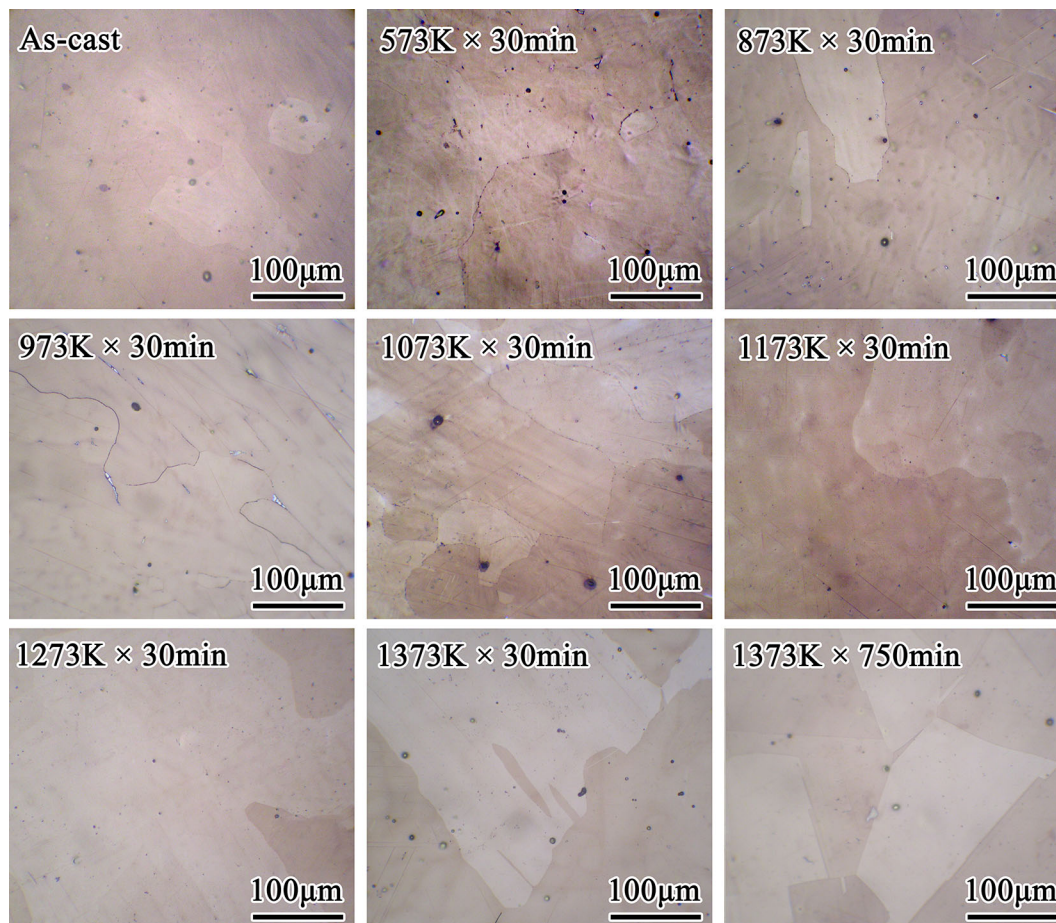
Fig. 1—Color optical micrographs of as-cast specimens before and after annealing at different temperatures for 30 min.

Figure 2 shows EBSD phase maps of austenite in an as-cast specimen as well as one annealed at 873 K (600 °C) for 30 minutes and another at 1373 K (1100 °C) for 750 minutes. Table II gives the densities of the twin boundaries, low-angle and high-angle grain boundaries based on the results of Figure 2. For the as-cast specimen and the one annealed at 873 K (600 °C) for 30 minutes, the density of twin boundaries was only 1.68 and 1.91 mm^{-1}, respectively. However, the density of twin boundaries increased remarkably to 3.86 mm^{-1} after annealing at 1373 K (1100 °C) for 750 minutes. In addition, a large amount of low-angle grain boundaries existed in the as-cast specimen. The low-angle grain boundaries were still abundant even after annealing at 873 K (600 °C) for 30 minutes. Nevertheless, the low-angle grain boundaries were substantially eliminated by annealing at 1373 K (1100 °C) for 750 minutes. The TEM results shown in Figure 3 reveal that an array of dislocations, indicated by white arrows, existed in addition to some stacking faults and random dislocations in the as-cast specimen. In addition, Table III shows that the stacking fault probability of the as-cast specimen substantially increased to 0.0184 from 0.0081 after annealing at 873 K (600 °C) for 30 minutes. When the annealing time of 873 K (600 °C) was further extended to 720 minutes, the stacking fault probability decreased to 0.0142. After annealing at 1073 K (800 °C) for 30 minutes, the stacking fault probability remained 0.0130. However, the stacking fault probability was only 0.0065 after annealing at 1373 K (1100 °C) for 30 minutes. Furthermore, the stacking fault probability further decreased to 0.0025 when the annealing time of 1373 K (1100 °C) was extended to 750 minutes.

Figure 4 shows color optical micrographs of as-cast specimens after annealing at 873 K (600 °C) for different times. The longer the annealing time is, the more precipitates are observed along grain boundaries. The SEM results in Figure 5 show that few particles precipitated along the grain boundaries in the as-cast specimen, whereas several particles were observed for the cast specimen annealed at 873 K (600 °C) for 720 minutes. Table IV indicates that the particles were enriched with Mn, Si, and Cr and depleted in Ni, and their chemical compositions were consistent with (Fe, Ni)$_{36}$(Mn, Si, Cr)$_{22}$. Stanford et al. also found (Fe, Ni)$_{36}$(Mn, Si, Cr)$_{22}$ particles along grain boundaries in a processed Fe-13.25Mn-5.05Si-8.70Cr-7.05Ni alloy subjected to heat treatment at 973 K (700 °C) for 240 minutes and confirmed that the particles were χ phase.[36] As a result, the particles in the annealed cast specimen were also χ phase.
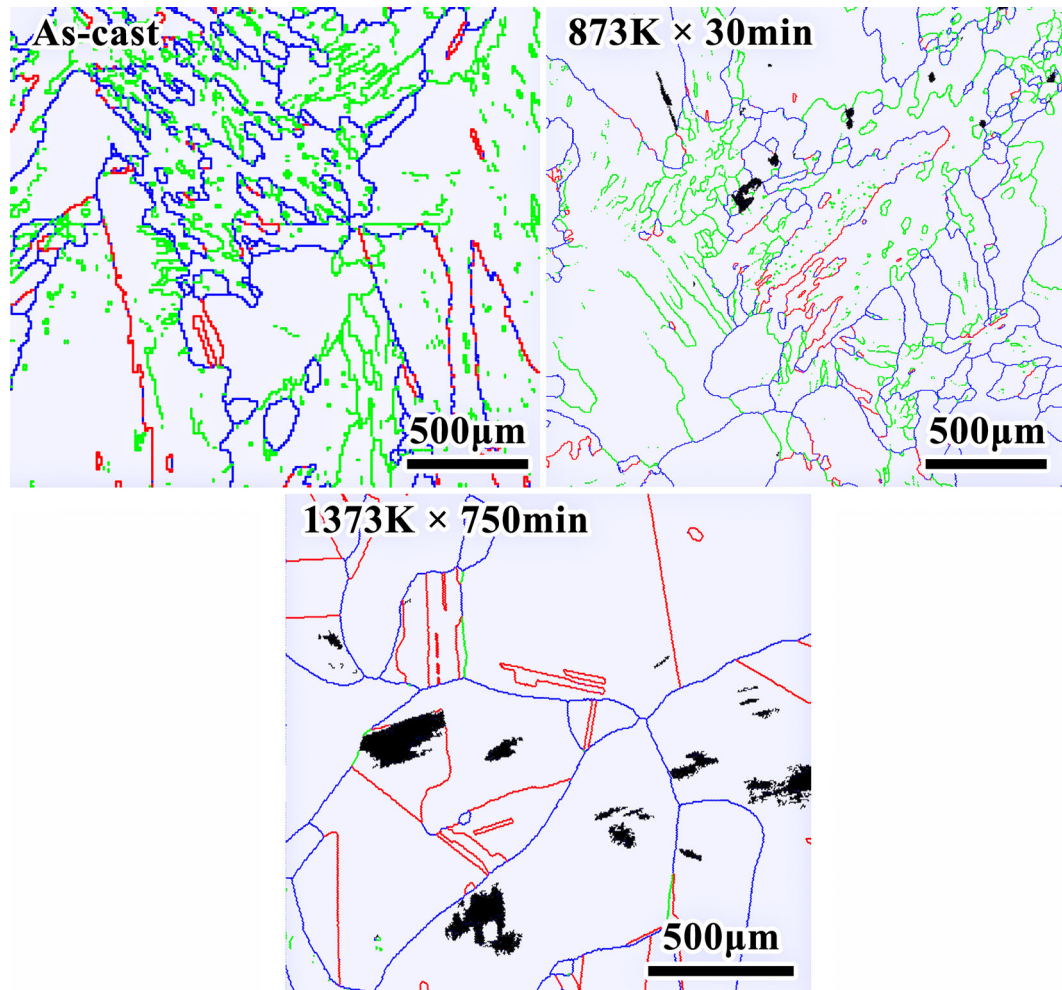
Fig. 2—EBSD phase maps of austenite in as-cast specimens before and after annealing at 873 K (600 °C) for 30 min or 1373 K (1100 °C) for 750 min. Blue lines are high-angle grain boundaries whose misorientation is greater than 15 deg. Green lines are low-angle grain boundaries whose misorientation is less than 15 deg. Red lines are twin boundaries (Color figure online).

B. Effect of Annealing Parameters on Stress-Induced Martensitic Transformation

Figures 6 and 7 show the XRD patterns of the as-cast specimens before and after annealing at different temperatures for different times when deformed by a 5-pct tensile strain at $M_s + 10$ K. For the as-cast and annealed specimens, both ε-martensite and γ-austenite were observed after deformation. The fraction of ε-martensite could be semiquantitatively calculated using the XRD patterns. Generally, the (10.1) peak of ε-martensite and (200) peak of γ-austenite are used to calculate the volume fraction of ε-martensite. However, the $(10.1)_\varepsilon$ and $(200)_\gamma$ peaks were abnormal owing to the coarse austenitic grains. For instance, the $(200)_\gamma$ peak nearly disappeared for the cast specimen annealed at 873 K (600 °C) for 30 minutes, as shown in Figures 6 and 7. The intensity of the $(200)_\gamma$ peak was even higher than that of the $(111)_\gamma$ peak for the cast specimen annealed at 573 K or 1073 K (300 °C or 800 °C) for 30 minutes, as shown in Figure 6. The intensity of the $(10.1)_\varepsilon$ peak was lower than that of the $(10.0)_\varepsilon$ peak for the cast specimen annealed at 873 K (600 °C) for

5 minutes, as shown in Figure 7. Therefore, the volume fraction of ε-martensite could not be calculated by the XRD patterns for all as-cast and annealed specimens.

Figure 8 shows color optical micrographs of an as-cast specimen and specimens annealed at different temperatures for different times when deformed by 5 pct tensile strain at $M_s + 10$ K. Different austenitic grains had different amounts of ε-martensite, and the larger the austenitic grains were, the greater the amount of ε martensite. In addition, the manual point counting method had to be employed to measure the volume fraction of ε-martensite because the XRD method could not determine the amount of ε-martensite for the as-cast and annealed specimens. Table V gives the volume fraction of ε-martensite that resulted from manually counting the ε-martensite points in the color optical micrographs shown in Figure 8. The volume fraction of the stress-induced ε-martensite was 41.6 pct in the as-cast specimen. After annealing at 573 K (300 °C) for 30 minutes, it increased to 47.4 pct. When the annealing temperature increased to 873 K (600 °C), the volume fraction of the stress-induced ε-martensite

Table II. Densities of Low-Angle and High-Angle Grain Boundaries and Twin Boundaries As Well As Austenitic Grain Size for As-Cast Specimens Before and After Annealing

Heat Treatment	Density of Low-Angle Grain Boundaries (mm^{-1})	Density of High-Angle Grain Boundaries (mm^{-1})	Density of Twin Boundaries (mm^{-1})	Austenitic Grain Size (μm)
As-Cast	8.25	10.36	1.68	597
Annealing at 873 K (600 °C) for 30 min	8.38	11.07	1.91	652
Annealing at 1373 K (1100 °C) for 750 min	0.28	8.58	3.86	499

The density of low-angle grain boundaries represents the ratio of the length of the low-angle grain boundaries relative to the analyzed area; the density of high-angle grain boundaries represents the ratio of the length of the high-angle grain boundaries relative to the analyzed area; the density of twin boundaries represents the ratio of the length of the twin boundaries relative to the analyzed area.
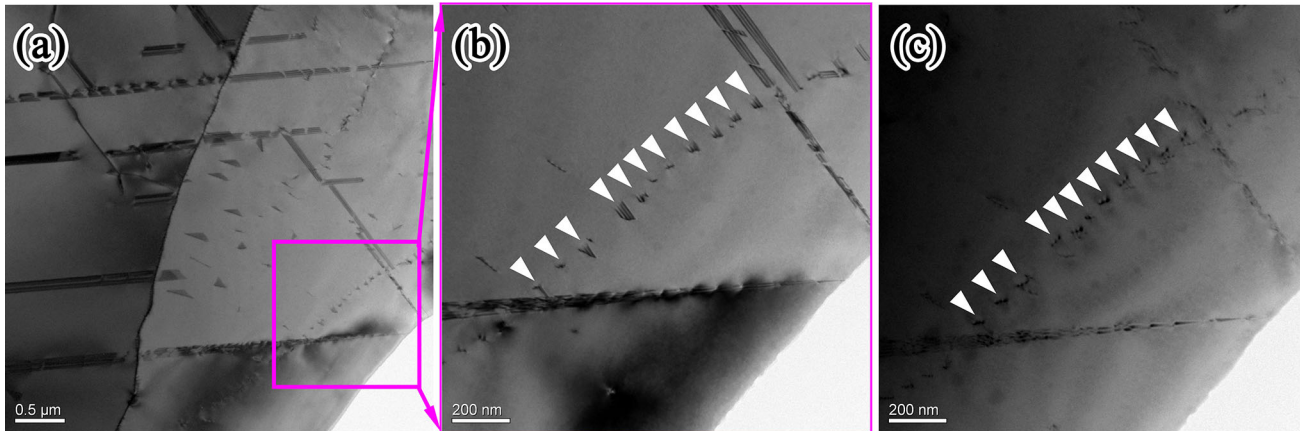

Fig. 3—TEM micrographs of an as-cast specimen where (*b*) is a partially enlarged view of (*a*), and (*c*) is the same area of (b) after the TEM specimen was rotated by a certain amount of degrees.

Table III. Stacking Fault Probabilities of As-Cast Specimens Before and After Annealing at Different Temperatures for Different Times

Heat Treatment	Stacking Fault Probability
Annealing at 573 K (300 °C) for 30 min	0.0122
Annealing at 873 K (600 °C) for 30 min	0.0184
Annealing at 873 K (600 °C) for 720 min	0.0142
Annealing at 1073 K (800 °C) for 30 min	0.0130
Annealing At 1373 K (1100 °C) for 30 min	0.0065
Annealing at 1373 K (1100 °C) for 750 min	0.0025

was further improved to 52.0 pct. However, it was only 39.5 pct when annealed at 1373 K (1100 °C) for 30 minutes. When the annealing temperature was fixed at 873 K (600 °C), the volume fraction of stress-induced ε-martensite after annealing for 720 minutes decreased to 42.3 pct from the 52.0 pct volume fraction that was present after annealing for 30 minutes.

C. *Effect of Annealing Parameters on Shape Memory Effect*

Figure 9 shows the relationship between deformation strain and recovery strain in as-cast specimens and those annealed at different temperatures for different times when the deformation temperature was M_s + 10 K. The recovery strain of the as-cast specimens exhibited a good shape memory effect, and their maximum recovery strain was 5.6 pct. The recovery strain was remarkably improved after annealing at 573 K (300 °C) for 30 minutes. In addition, the increase in the recovery strain was higher after annealing at 873 K (300 °C) than that at 573 K (300 °C), especially for a large deformation strain. Note that the former maximum recovery strain reached 7.7 pct. Upon increasing the annealing temperature to 1073 K (800 °C), the recovery strain still improved compared with that of the as-cast specimen. However, the improvement in the recovery strain was slightly lower after annealing at 1073 K (800 °C) than that at 573 K (300 °C). The recovery strain after annealing at 1373 K (1100 °C) for 30 minutes was even lower than that of the as-cast specimen when the deformation strain was above 7 pct. Upon extending the annealing time of 1373 K (1100 °C) to 750 minutes, the recovery strain declined dramatically, and its maximum value was only 4.3 pct.

Figure 10 shows the effect of annealing time on the shape memory effect of the as-cast specimens when the annealing temperature was 873 K (600 °C). The recovery strain of the as-cast specimens was improved by annealing at 873 K (600 °C) for only 5 minutes, and its maximum value was 7.1 pct. When the annealing time was extended to 30 minutes, the maximum recovery strain increased to 7.7 pct. Meanwhile, the recovery strain at 5 minutes was almost the same as that at 30 minutes when the deformation strain was below 9 pct. When further extending the annealing time to 720 minutes, the recovery strain was still higher than that of the as-cast specimens, and its maximum value was 6.3 pct. However, the increment of recovery strain was much less after annealing for 720 minutes than for 5 or 30 minutes.

IV. DISCUSSION

The SME in Fe-Mn-Si-based SMAs is, admittedly, associated with the stress-induced martensitic transformation from γ-austenite to ε-martensite and its reverse transformation.[3,37] It is self-evident that all factors that facilitate the stress-induced $\gamma \rightarrow \varepsilon$ martensitic transformation and suppressed dislocation glide during straining are beneficial to improving the SME. Recently, our research group reviewed the factors of achieving a large recovery strain of above 6 pct in polycrystalline Fe-Mn-Si-based SMAs.[3,32] In the case of microstructure design, three conditions, i.e., the presence of coarse austenitic grains, a high density of stacking faults, and a low density of twin boundaries, are in favor of obtaining

Table IV.   Chemical Compositions of Two Regions in Fig. 5(c)

Region	Elements (Wt Pct)				
	Mn	Si	Cr	Ni	Fe
A	19.26	6.16	8.92	5.09	bal.
B	18.20	5.03	8.61	5.81	bal.

Fig. 6—XRD patterns of an as-cast specimen and specimens annealed at different temperatures for 30 min after 5 pct tensile deformation at M_s + 10 K.
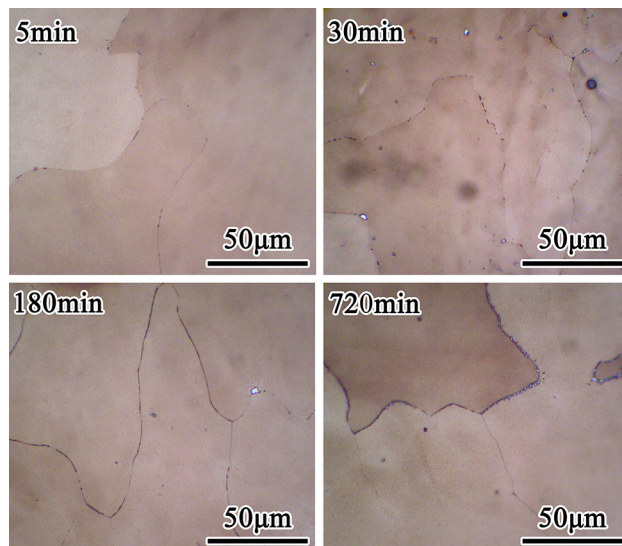

Fig. 4—Color optical micrographs of as-cast specimens after annealing at 873 K (600 °C) for different times.
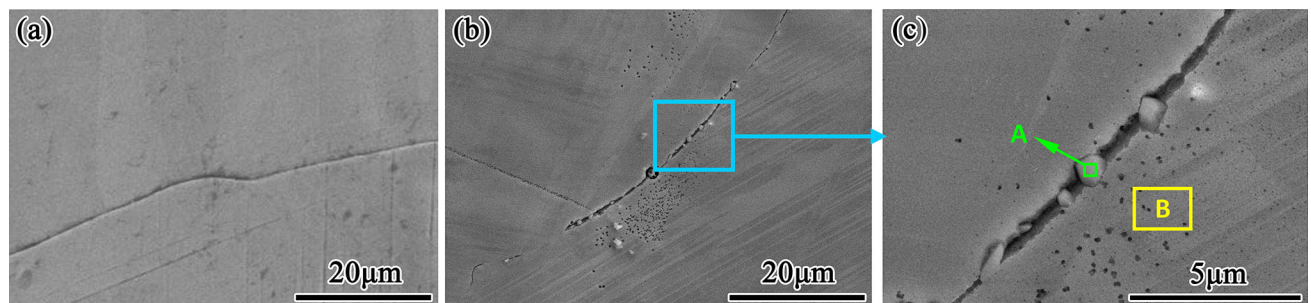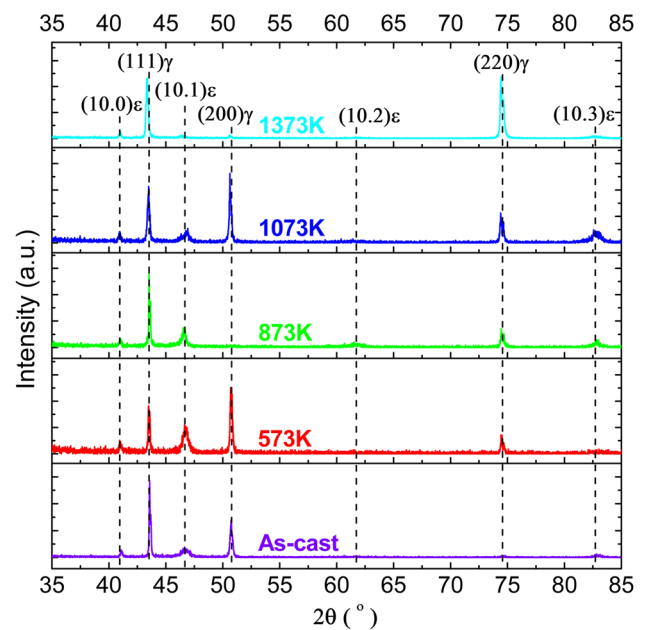

Fig. 5—(a) SEM micrographs of an as-cast specimen, (b) specimen subjected to annealing at 873 K (600 °C) for 720 min as well as (c) its partially enlarged view.
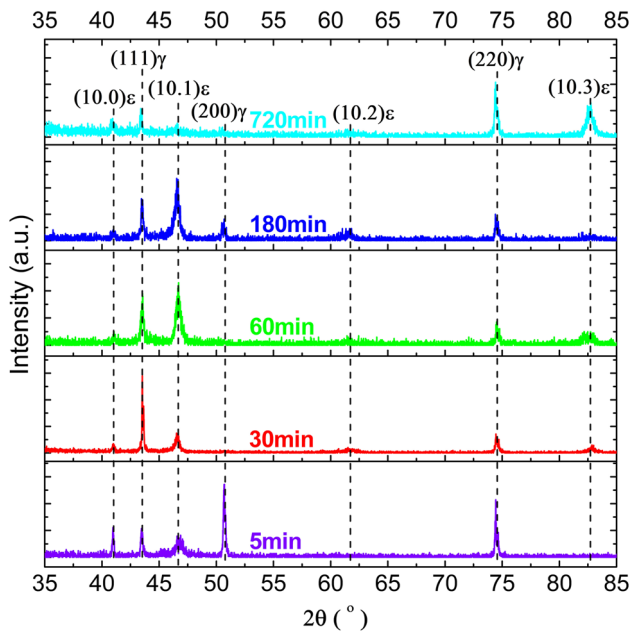
Fig. 7—XRD patterns of as-cast specimens annealed at 873 K (600 °C) for different times after 5 pct tensile deformation at $M_s + 10$ K.

the large recovery strain. For processed Fe-Mn-Si-based SMAs, both the high density of stacking faults and the low density of twin boundaries could be achieved by training, thermomechanical treatment, or ausforming.[3,27] However, the recovery strain of the processed Fe-Mn-Si-based SMAs could only be improved to approximately 5 pct by the above treatments because the austenitic grains, which are generally below 300 μm, are not large enough.[3,32] In the present paper, the austenitic grains in the as-cast specimens were 597 μm, which is much larger than that of the processed Fe-Mn-Si-based SMAs. Furthermore, the density of the twin boundaries was one order of magnitude less in the as-cast specimens than that in the solution-treated-processed Fe-Mn-Si-based SMAs (i.e., > 24 mm^{-1}[38]). This means that the as-cast specimens satisfied two of the conditions, i.e., the presence of coarse austenitic grains and low-density twin boundaries (Figure 2 and Table II), but did not satisfy the condition of high-density stacking faults being present (Figure 3). In this case, the maximum recovery strain of the as-cast specimens only achieved 5.6 pct. This implies that the three conditions of microstructure design should be satisfied simultaneously for the purpose of achieving a large recovery strain above 6 pct.

Compared with the as-cast specimens, the shape memory effect of the annealed cast specimens was increased to varying degrees or even deteriorated depending on the annealing processes (Figures 9 and 10). Generally, annealing plays an important role in alleviating or eliminating the microsegregation of castings. Accordingly, it seems that the evolution of the shape memory effect with annealing processes is associated with the alleviation of microsegregation for cast Fe-Mn-Si-based SMAs. However, the shape memory

effect of the as-cast specimens could be remarkably improved by annealing at 573 K (300 °C) for 30 minutes or at 873 K (600 °C) for 5 minutes (Figures 9 and 10), although the microsegregation was not substantially reduced by either of the above annealing processes. As a result, the evolution of microsegregation during annealing is not the key factor affecting the shape memory effect of cast Fe-Mn-Si-based SMAs.

A large amount of low-angle grain boundaries existed in the as-cast specimens (Figure 2). An array of dislocations could form a low-angle grain boundary according to dislocation model. The TEM results revealed that an array of dislocations appeared in the as-cast specimens (Figure 3). It was deduced that the low-angle grain boundaries in the as-cast specimens should consist of dislocations. Moreover, after annealing at a sufficient temperature, the perfect dislocations could split into Shockley partial dislocations, thereby forming stacking faults with respect to the Fe-Mn-Si-based SMAs.[39,40] Note that the density of the low-angle grain boundaries for the as-cast specimens was almost the same before and after annealing at 873 K (600 °C) for 30 minutes (Figure 2 and Table II), while the stacking fault probability significantly increased to 0.0184 from 0.0081 (Table III). This further demonstrated that these dislocations originated from the low-angle grain boundaries and decomposed into stacking faults after sufficient annealing. In addition, stress-induced ε-martensite preferentially nucleates and grows at stacking faults, and thus the shape memory effect could be improved by introducing stacking faults.[3,37] Meanwhile, dislocations and stacking faults can be eliminated by annealing in addition to microsegregation. Accordingly, the variation of the shape memory effect with annealing processes was mainly related to the evolution of dislocations in the cast Fe-Mn-Si-based SMAs.

After annealing at 573 K (300 °C) for 30 minutes, some dislocations decomposed into stacking faults (Table III), and the stress-induced ε-martensite transformation was promoted to some extent. As a result, the volume fraction of stress-induced ε-martensite increased to 47.4 pct from 41.6 pct in the as-cast specimens (Figure 8 and Table V) and the shape memory effect was improved after annealing at 573 K (300 °C) for 30 minutes (Figure 9). When further increasing the annealing temperature to 873 K (600 °C), the stacking fault probability dramatically increased to 0.0184 from 0.0081 in the as-cast specimens (Table III). It was demonstrated that the dislocations were easier to split into stacking faults. As a consequence, after annealing at 873 K (600 °C) for 30 minutes, the quantity of stress-induced ε-martensite was the highest among all annealed cast specimens (Figure 8 and Table V), and the best shape memory effect was obtained (Figures 9 and 10). In addition, the stacking fault probability decreased to 0.0130 after annealing at 1073 K (800 °C) for 30 minutes, and it was only 0.0065 after annealing at 1373 K (1100 °C) for 30 minutes. This result indicated that the amount of dislocations decreased because the annealing temperature was too high, which resulted in a decrease in the stacking faults. Therefore, the volume fraction of stress-induced ε-martensite in the cast
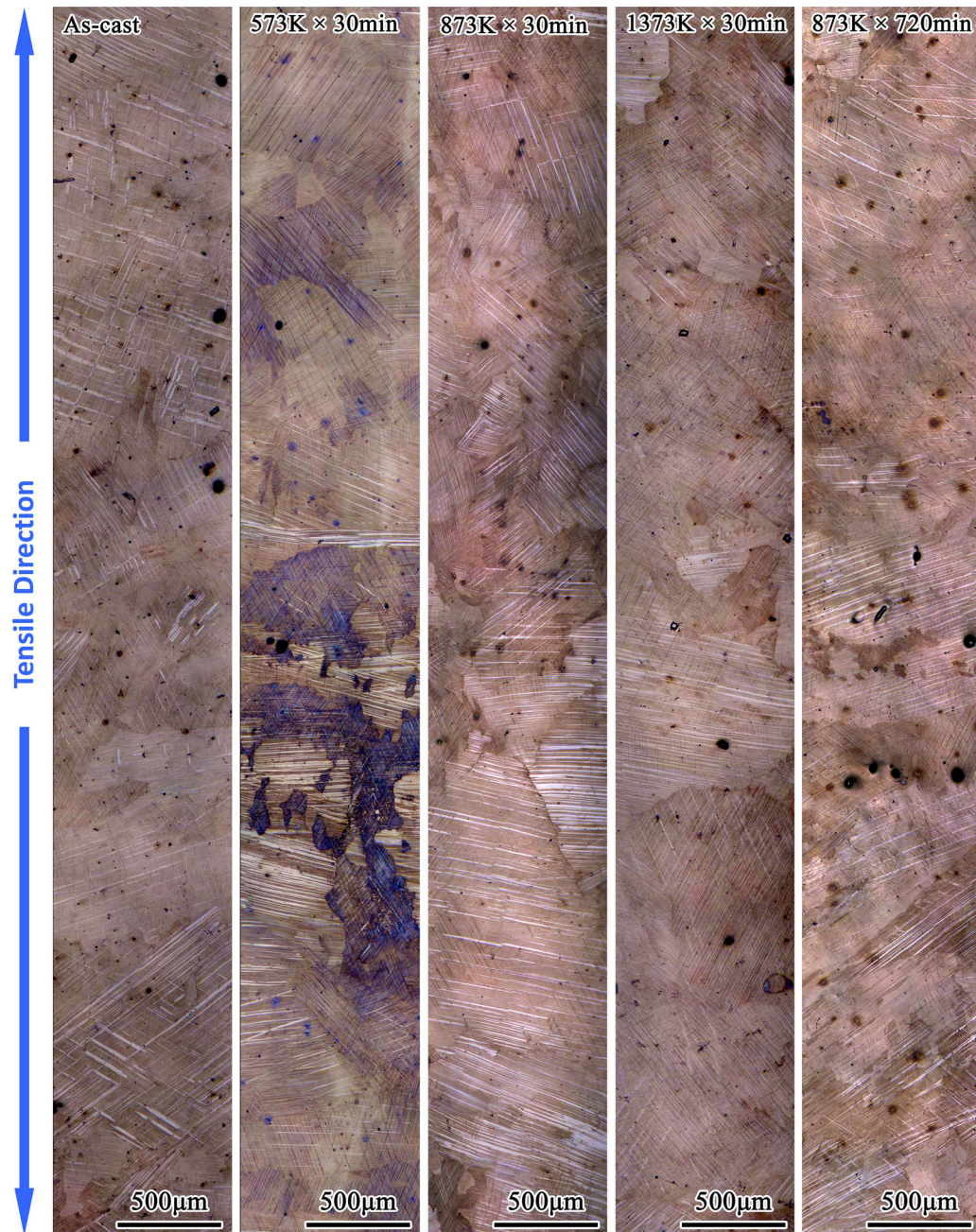
Fig. 8—Color optical micrographs of an as-cast specimen and specimens annealed at different temperatures for different times after 5 pct tensile deformation at M_s + 10 K.

Table V. Volume Fractions of Stress-Induced ε-Martensite for As-Cast Specimens Before and After Annealing at Different Temperatures for Different Times When Deformed by 5 Pct Tensile Strain at M_s + 10 K

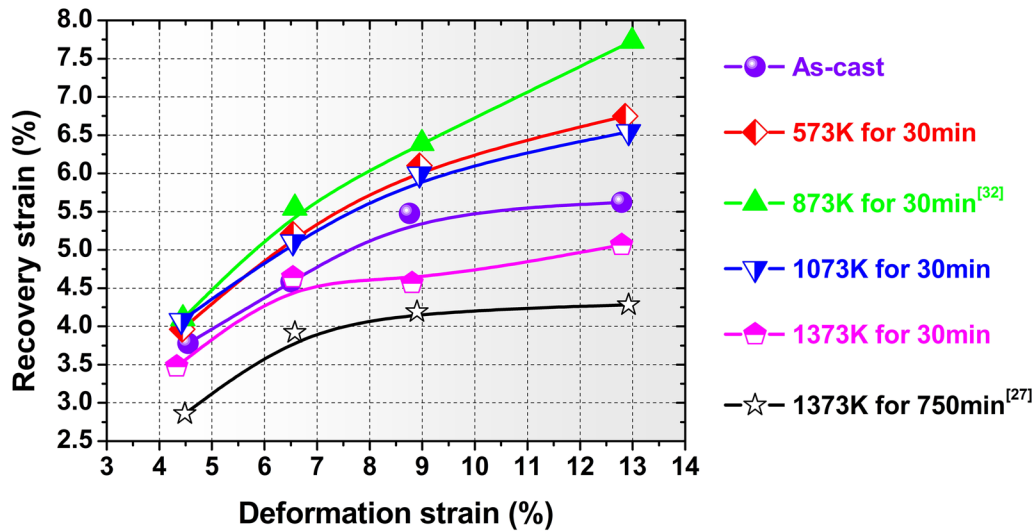| Heat Treatment	Volume Fraction of ε-Martensite (Pct)
As-Cast	41.6
Annealing at 573 K (300 °C) for 30 min	47.4
Annealing at 873 K (600 °C) for 30 min	52.0
Annealing at 1373 K (1100 °C) for 30 min	39.5
Annealing at 873 K (600 °C) for 720 min	42.3

Fig. 9—Recovery strains as a function of deformation strains for as-cast specimens and specimens annealed at different temperatures for 30 min when the deformation temperature was M_s + 10 K.
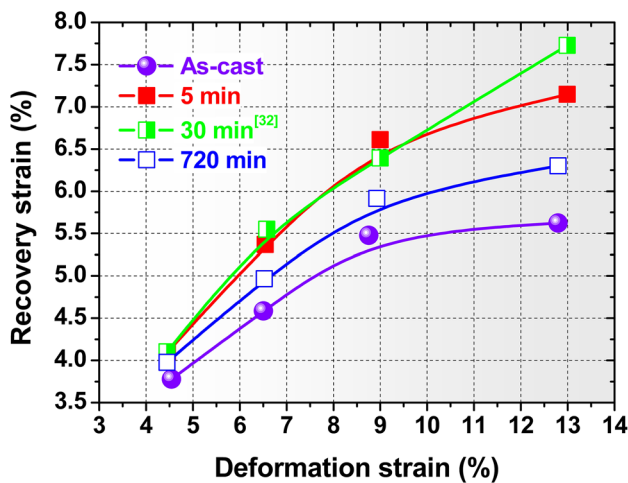

Fig. 10—Recovery strains as a function of deformation strains for as-cast specimens and specimens annealed at 873 K (600 °C) for different times when the deformation temperatures were M_s + 10 K.

specimens annealed at 1373 K (1100 °C) for 30 minutes decreased to 39.5 pct from 41.6 pct in the as-cast specimens. In this case, the shape memory effect deteriorated after annealing at 1373 K (1100 °C) for 30 minutes. When further extending the annealing time at 1373 K (1100 °C) to 750 minutes, the density of twin boundaries increased remarkably (Figure 2 and Table II), and the stacking fault probability was only 0.0025 due to the elimination of a large number of low-angle grain boundaries (Figure 2 and Table III). As mentioned above, the introduction of twin boundaries and decrease in stacking faults are harmful to the shape memory effect of Fe-Mn-Si-based SMAs.[3] Accordingly, the shape memory effect of the cast specimens annealed at 1373 K (1100 °C) for 750 minutes was the worst among all annealed cast specimens.

In the case of annealing at 873 K (600 °C) for different times, the annealing time was too short to adequately facilitate the transformation of dislocations to stacking faults. Thus, the shape memory effect was slightly worse after annealing at 873 K (600 °C) for 5 minutes than that for 30 minutes. On the other hand, the amount of dislocations should decrease more rapidly upon extending the annealing time, thereby resulting in a decrease in the amount of stacking faults. Indeed, the stacking fault probability was smaller after annealing for 720 minutes than that for 30 minutes (Table III). As a result, the volume fraction of stress-induced ε-marten-site decreased to 42.3 pct from 52.0 pct for annealing times of 720 and 30 minutes, respectively. Thus, an improvement in the shape memory effect was much lower when the annealing time was 720 minutes compared to that for 30 minutes. In addition, the amount of χ phase increased with annealing time (Figures 4 and 5). However, the χ phase precipitated mainly along the grain boundaries and thus had a negligible effect on the shape memory effect.

V. CONCLUSIONS

1. A large amount of low-angle grain boundaries consisting of dislocations existed in the as-cast Fe-18.54Mn-5.70Si-8.91Cr-4.45Ni shape memory alloy. The variation of its shape memory effect with different annealing processes was mainly associated with the evolution of dislocations derived from low-angle grain boundaries.
2. For the as-cast Fe-18.54Mn-5.70Si-8.91Cr-4.45Ni alloy, the maximum improvement in the shape memory effect was achieved after annealing at 873 K (600 °C) for 30 minutes when the annealing temperature range was from 573 K to 1373 K

(300 °C to 1100 °C) and the range for the annealing time was from 5 to 750 minutes in this work.
3. The recovery strain of the as-cast Fe-18.54Mn-5.70-Si-8.91Cr-4.45Ni alloy was only 5.6 pct because coarse austenitic grains and a low density of twin boundaries were present, whereas a high density of stacking faults was not present. After annealing at 873 K (600 °C) for 30 minutes, the recovery strain was significantly improved to 7.7 pct because dislocations derived from low-angle grain boundaries decomposed into stacking faults.

REFERENCES

1. A. Sato, E. Chishima, K. Soma, and T. Mori: *Acta Metall.*, 1982, vol. 30, pp. 1177–83.
2. H. Otsuka, H. Yamada, T. Maruyama, H. Tanahashi, S. Matsuda, and M. Murakami: *ISIJ Int.*, 1990, vol. 30, pp. 674–79.
3. H. Peng, J. Chen, Y. Wang, and Y. Wen: *Adv. Eng. Mater.*, 2018, p. 1700741.
4. A. Sato, E. Chishima, Y. Yamaji, and T. Mori: *Acta Metall.*, 1984, vol. 32, pp. 539–47.
5. A. Sato and T. Mori: *Mater. Sci. Eng. A*, 1991, vol. 46, pp. 197–204.
6. Y. Watanabe, Y. Mori, and A. Sato: *J. Mater. Sci.*, 1993, vol. 28, pp. 1509–14.
7. C.Y. Chung, C. Shuchuan, and T.Y. Hsu: *Mater. Charact.*, 1996, vol. 37, pp. 227–36.
8. A. Baruj, T. Kikuchi, S. Kajiwara, and N. Shinya: *Mater. Sci. Eng. A*, 2004, vol. 378, pp. 333–36.
9. N. Stanford and D.P. Dunne: *Mater. Sci. Eng. A*, 2006, vol. 422, pp. 352–59.
10. C.H. Yang, H.C. Lin, K.M. Lin, and H.K. Tsai: *Mater. Sci. Eng. A*, 2008, vol. 497, pp. 445–50.
11. V. Fuster, A.V. Druker, A. Baruj, J. Malarría, and R. Bolmaro: *Mater. Charact.*, 2015, vol. 109, pp. 128–37.
12. L.J. Rong, Y.Y. Li, and C.X. Shi: *Mater. Lett.*, 1994, vol. 21, pp. 395–97.
13. L.J. Rong, Y.Y. Li, and C.X. Shi: *Scr. Mater.*, 1996, vol. 34, pp. 993–98.
14. O. Matsumura, S. Furusako, T. Sumi, T. Furukawa, and H. Otsuka: *Mater. Sci. Eng. A*, 1999, vol. 272, pp. 459–62.
15. D. Wang, D. Liu, Z. Dong, W. Liu, and J. Chen: *Mater. Sci. Eng. A*, 2001, vol. 315, pp. 174–79.
16. N. Stanford, K. Chen, D.P. Dunne, and X.J. Jin: *ISIJ Int.*, 2007, vol. 47, pp. 883–89.
17. K. Tsuzaki, Y. Natsume, Y. Kurokawa, and T. Maki: *Scr. Metall. Mater.*, 1992, vol. 27, pp. 471–73.
18. C.H. Yang, H.C. Lin, K.M. Lin, and W.H. Ho: *Mater. Trans.*, 2008, vol. 49, pp. 1853–57.
19. C.P. Wang, Y.H. Wen, H.B. Peng, D.Q. Xu, and N. Li: *Mater. Sci. Eng. A*, 2011, vol. 528, pp. 1125–30.
20. S. Kajiwara, D. Liu, T. Kikuchi, and N. Shinya: *Scr. Mater.*, 2001, vol. 44, pp. 2809–14.
21. Z.Z. Dong, S. Kajiwara, T. Kikuchi, and T. Sawaguchi: *Acta Mater.*, 2005, vol. 53, pp. 4009–18.
22. Y.H. Wen, W. Zhang, N. Li, H.B. Peng, and L.R. Xiong: *Acta Mater.*, 2007, vol. 55, pp. 6526–34.
23. N. Stanford and D.P. Dunne: *J. Mater. Sci.*, 2006, vol. 41, pp. 4883–91.
24. A. Druker, P. La Roca, P. Vermaut, P. Ochin, and J. Malarría: *Mater. Sci. Eng. A*, 2012, vol. 556, pp. 936–45.
25. J.C. Li, X.X. Lü, and Q. Jiang: *ISIJ Int.*, 2000, vol. 40, pp. 1124–26.
26. H. Kubo, H. Otsuka, S. Farjami, and T. Maruyama: *Scr. Mater.*, 2006, vol. 55, pp. 1059–62.
27. Y.H. Wen, H.B. Peng, D. Raabe, I. Gutierrez-Urrutia, J. Chen, and Y.Y. Du: *Nat. Commun.*, 2014, vol. 5, p. 4964.
28. H.B. Peng, G.X. Wang, Y.Y. Du, S.L. Wang, J. Chen, and Y.H. Wen: *Metall. Mater. Trans. A*, 2016, vol. 47A, pp. 3277–83.
29. H.B. Peng, Y.H. Wen, Y.Y. Du, Q.X. Yu, and Q. Yang: *Metall. Mater. Trans. B*, 2013, vol. 44B, pp. 1137–43.
30. H.B. Peng, Y.H. Wen, Y.Y. Du, J. Chen, and Q. Yang: *Metall. Mater. Trans. B*, 2014, vol. 45B, pp. 6–11.
31. G.X. Wang, H.B. Peng, P.P. Sun, S.L. Wang, and Y.H. Wen: *Mater. Sci. Eng. A*, 2016, vol. 657, pp. 339–46.
32. H. Peng, G. Wang, S. Wang, J. Chen, I. MacLaren, and Y. Wen: *Mater. Sci. Eng. A*, 2018, vol. 712, pp. 37–49.
33. Y.H. Wen, H.B. Peng, P.P. Sun, G. Liu, and N. Li: *Scr. Mater.*, 2010, vol. 62, pp. 55–58.
34. Y.H. Wen, H.B. Peng, C.P. Wang, Q.X. Yu, and N. Li: *Adv. Eng. Mater.*, 2011, vol. 13, pp. 48–56.
35. Y. Rong, G. He, Z. Guo, S. Chen, and T.Y. Hsu: *J. Mater. Sci. Technol.*, 2002, vol. 5, p. 5.
36. N. Stanford, D. Dunne, and B. Monaghan: *J. Alloys Compd.*, 2007, vol. 430, pp. 107–15.
37. S. Kajiwara: *Mater. Sci. Eng. A*, 1999, vols. 273–275, pp. 67–88.
38. G.X. Wang, H.B. Peng, C.Y. Zhang, S.L. Wang, and Y.H. Wen: *Smart Mater. Struct.*, 2016, vol. 25, p. 075013.
39. J. Li and C.M. Wayman: *Scr. Metall.*, 1992, vol. 27, pp. 279–84.
40. B. Jiang, T. Tadaki, H. Mori, and T.Y. Hsu: *Mater. Trans.*, 1997, vol. 38, pp. 1078–82.